Chapter 8

Silicon-Germanium (SiGe) Nanostructures for Thermoelectric Devices: Recent Advances and New Approaches to High Thermoelectric Efficiency

Jaime Andrés Pérez-Taborda,
Olga Caballero-Calero and Marisol Martín-González

Additional information is available at the end of the chapter

http://dx.doi.org/10.5772/67730

Abstract

Silicon and germanium present distinct and interesting transport properties. However, composites made of silicon-germanium (SiGe) have resulted in a breakthrough in terms of their transport properties. Currently, these alloys are used in different applications, such as microelectronic devices and integrated circuits, photovoltaic cells, and thermoelectric applications. With respect to thermoelectricity, in the last decades, $Si_{0.8}Ge_{0.2}$ has attracted significant attention as an energy harvesting material, for powering space applications and other industrial applications. This chapter focuses on the recent advances and new approaches in silicon-germanium ($Si_{1-x}Ge_x$) nanostructures for thermoelectric devices with high thermoelectric efficiency obtained through magnetron sputtering.

Keywords: silicon-germanium nanostructures, magnetron sputtering deposition, thin films, nanomesh, thermoelectric, Raman spectroscopy

1. Introduction

Several chapters of this book describe different approaches, properties, and applications of silicon and its undeniable impact on our culture, technology, and commerce. Its usefulness has made us talk about the silicon era [1]. In this chapter, we are going to focus on the use of silicon-based materials in one of the main pillars of our life nowadays: the obtainment of energy to power up all the resources in which our society is based (transport, communications, and human infrastructures in general).

Although silicon is mainly associated with microchip devices and advances in computing, the alloy that silicon forms with germanium can be used as a thermoelectric material, which is, in the presence of a gradient of temperature, able to generate an electrical voltage and *vice versa*. This thermoelectric effect has been long known. Nevertheless, it has not been widely used because of its modest efficiency. In recent years, the interest on thermoelectricity has revamped due to the use of thermoelectric devices for micro-energy harvesting or as a large-scale conversion of residual heat into electricity. This increase in the research on thermoelectrics is mostly due to the impact nanostructuration has on improving the efficiency of these materials, which has been increased almost a factor of three over the last 20 years. The purpose of this chapter is to highlight the ways in which silicon-germanium has improved its efficiency by nanostructuration.

Considering the decreasing fossil fuels and increasing energy demand worldwide, a pressing need for improved direct thermal (wasted heat) into electrical energy conversion is imposed. The wasted heat comes from the energy transportation, vehicles, electricity generating sources, industry, etc., which tampers the actual efficiency of the initial resources. For instance, around 30% of the energy obtained from the fuel of a car is actually used in its movement. The other 70% is lost in the form of heat, friction, and cooling the car. Furthermore, it is completely reasonable to look for alternative energy technologies to reduce our dependence on fossil fuels and greenhouse gas effects. This necessity has fostered multiple lines of research, including the conversion of thermal energy through thermoelectricity [2]. As an example, the most recent International Energy Outlook 2016 (IEO2016) [3] prepared by the USA Energy Information Administration shows the energy production predictions for the year 2040, based on the data recorded previously (**Figure 1a**). It is shown that the total world consumption of energy will increase a 48% from 2012 to 2040. Renewable energies are the fastest-growing energy sources over the predicted period, with a foreseen increase in their consumption of around 2.6%/year between 2012 and 2040. In **Figure 1a**, CPP refers to a Clean Power Plan (CPP), which is a USA regulation that aims to reduce carbon dioxide emissions from electric power generation by 32% within 25 years, relative to the levels of 2005 in the USA.

Focusing on the future of the different sources of energies, that is **Figure 1b**, world net electricity generation is envisioned to increase by 69%, in 2040, going from 21.6 trillion kilowatt hours (10^{12} kWh) registered in 2012 to 25.8 trillion kWh predicted for 2020 and to 36.5 trillion kWh in 2040. It is worth noting that, even with initiatives as the CPP, or the development predicted for renewable energies, fossil fuels will still account for a 78% of the energy used in 2040 [3].

For these reasons, in late 2015, representatives from 185 countries and the European Union (EU) met in Paris to reach a commitment to addressing climate change, called Paris-COP21. This worldwide engagement is expected to drive innovation in renewable energies, battery storage, energy efficiency, and energy recovery. One of the main conclusions obtained in the conference is that climate change is often discussed as a single problem, but solving it will require a wide variety of solutions [4]. The EU budget for low carbon-related research under Horizon 2020 has been effectively doubled for the period 2014–2020, and the EU has promised to invest at least 35% of Horizon 2020 resources into climate-related activities [5]. In the United States, hundreds of major companies, including energy-related companies such as ExxonMobil, Shell, DuPont, Rio Tinto, Berkshire Hathaway Energy, Cal-pine, and Pacific Gas and Electric Company, have supported the Paris-COP21 [6]. In the coming decades, there will be a need for more energy-efficient technologies, easily compatible with the non-renewable

http://dx.doi.org/10.5772/67730

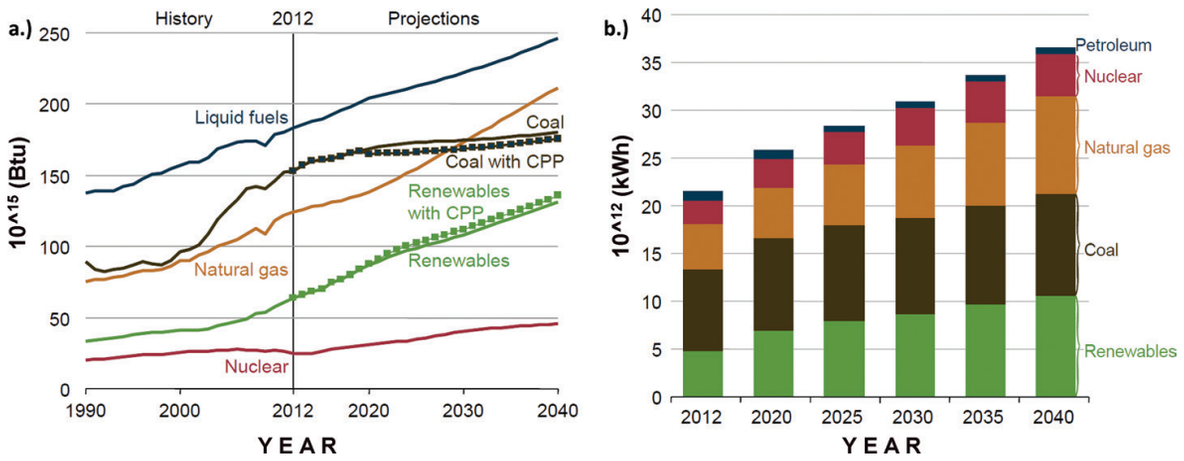

Figure 1. (a) Total world energy consumption sorted by energy source between the period 1990 and 2040. Dotted lines for coal (black) and renewables (green) show the predicted effects of the USA Clean Power Plan (CPP) regulation. (b) World net electricity generation predictions sorted by energy source, for the period of 2012–2040. Both figures are reprinted with permission from Ref. [3]. Copyright 2016.

energies (that will not disappear in the near future as it can be seen in **Figure 1b**). Certainly, thermoelectric materials and especially thin films are interesting players in this scenario. Its ability to convert waste heat into electricity regardless of the source of heat generation, stability over time, and the ability to generate electricity locally without the need for transportation are some of its many advantages.

Likewise, **Figure 2** and **Table 1** show some of the most outstanding historical facts and current state of the art of Si and SiGe in thermoelectric, microelectronic, and photovoltaic applications.

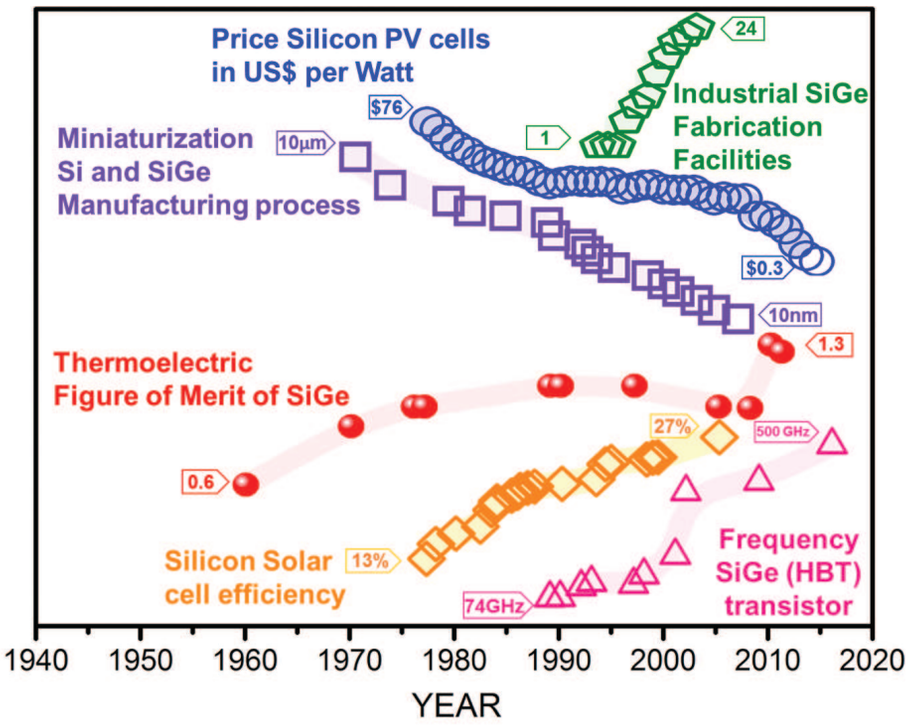

Figure 2. Timeline of some breakthrough or historical event in Si-Ge in thermoelectric, photovoltaic cells and microelectronics. References in **Table 1**.

	Some breakthrough or historical event in SiGe	Year	Refs
Microelectronics and Manufacturing	First epitaxial silicon transistors	1960	[7]
	First oxidation study of SiGe	1971	[8]
	First SiGe n-type MODFET	1986	[9]
	First SiGe p-type MODFET	1986	[10]
	First SiGe photodetector	1986	[11]
	First SiGe HBT (heterojunction bipolar transistor)	1987	[12]
	First SiGe hole RTD (resonant-tunneling diode)	1988	[13]
	First SiGe (BiCFET) (bipolar inversion channel FET)	1989	[14]
	First SiGe HBT grown by CVD (chemical vapor deposition)	1989	[15]
	First SiGe gate (CMOS) technology	1990	[16]
	First SiGe waveguide	1990	[17]
	First SiGe LED	1991	[18]
	First SiGe solar cell	1992	[19]
	First SiGe phototransistor	1993	[20, 21]
	First SiGe HBT with peak cutoff frequency above 100 GHz	1993	[22]
	First SiGe HBT with peak cutoff frequency above 200 GHz	2001	[23]
	First SiGe HBT with peak cutoff frequency above 300 GHz	2002	[7]
	Current Record SiGe HBT with peak cutoff frequency 500 GHz	2016	[24]
Thermoelectric figure of merit	SiGe radioisotope thermoelectric generators (RTGs) Mission LES 8, 9	1976	*[25–28]*
	SiGe (RTGs) in mission Voyager 1 and 2 spacecraft	1977	[25–27]
	SiGe (RTGs) in mission Galileo spacecraft	1989	[25–27, 29]
	SiGe (RTGs) in mission Ulysses spacecraft	1990	[25–27, 29]
	SiGe (RTGs) in mission Cassini spacecraft	1997	[25, 26]
	SiGe (RTGs) in mission New Horizons spacecraft	2005	[25–27]
	Bulk material (zT)~ 1.3 at 1073 K	2014	[30]
	Historical evolution zT SiGe	2016	[31, 32]

http://dx.doi.org/10.5772/67730

	Some breakthrough or historical event in SiGe	Year	Refs
✹	% Solar cell efficiency	1998	[33]
		2003	[34]
		2014	[35]
		2015	[36, 37]
		2016	[38]
$	Price history photovoltaic cells in US$ per watt	2012	[39–41]
		2015	[42, 43]
↓	Recent progress of the miniaturization of semiconductors Si and SiGe	1988	[44]
		2000	[45]
		2004	[46]
		2010	[47]
↑	Number of industrial SiGe and strained Si fabrication facilities	2000	[48]
		2007	[49]

Table 1. This table highlights historical events and the latest advances in silicon and silicon-germanium in thermoelectric, microelectronic, and photovoltaic applications.

2. Thermoelectric concepts: current overview and strategies for improving the thermoelectric efficiency

The efficiency of a thermoelectric material is controlled by its figure of merit, denoted as zT. This parameter is defined as follows:

$$zT = \alpha^2 \cdot \sigma \cdot T \cdot \kappa^{-1} \tag{1}$$

where the parameters are the following: the square of the Seebeck coefficient, α, times the electrical conductivity, σ, times the operating temperature, T (in Kelvin), divided by the thermal conductivity, κ. The thermal conductivity itself is a sum of its lattice and electronic contributions, κ_L and κ_e, respectively.

Most of these parameters are heavily interdependent [50–53], as it is shown in **Figure 3**. If one takes into account the material properties in classical physics, large α usually results in a low σ, and a large σ increases κ_e, given that these parameters depend on the carrier concentration. Therefore, the fabrication of materials with high power factor ($\alpha^2 \cdot \sigma$) and low thermal conductivity (κ) necessary for obtaining a high zT is quite challenging. The energy conversion efficiency (η_{max}) of thermoelectric devices is determined by Eq. (2), with T_H and T_C being the hot and cold temperatures, respectively.

$$n_{max} = \frac{T_H - T_C}{T_H} \frac{\sqrt{1+ZT}-1}{\sqrt{1+ZT}+\frac{T_C}{T_H}} \tag{2}$$

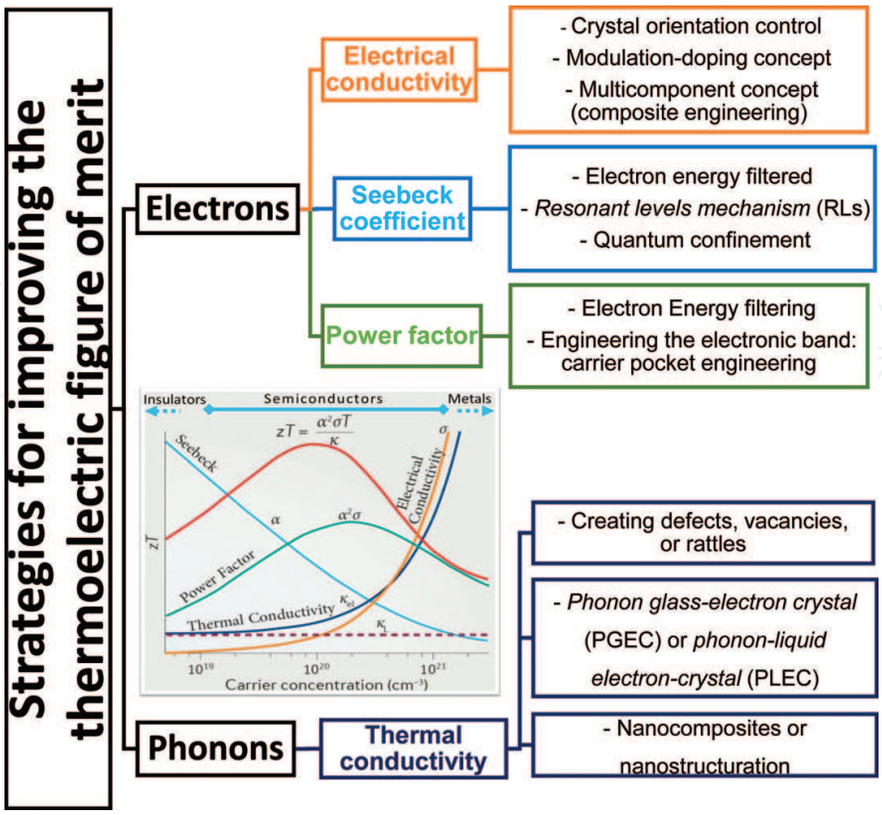

Figure 3. Schematic diagram that briefly summarizes some of the main strategies for the improvement of the figure of merit through the increase in the power factor and the decrease in the thermal conductivity. The graph shows the behavior of the Seebeck coefficient, electrical conductivity, and thermal conductivity versus carrier concentration. This figure is adapted from Ref. [50].

As it can be seen from the definition of the figure of merit, a large value of zT can be obtained by having a high power factor ($\alpha^2 \cdot \sigma$) and a low thermal conductivity (κ). In **Figure 3**, there is also a scheme with some of the strategies that are being used nowadays to improve the figure of merit.

As it can be seen in **Figure 3**, there are two main routes to improve the thermoelectric figure of merit, which are tailoring to improve the power factor and lowering the thermal conductivity. In the first case, there have been different ideas proposed recently. Some of them are aimed to increase the Seebeck coefficient, such as quantum confinement in low-dimensional structures, which was first proposed by Hicks and Dresselhaus in 1993 [54]. It is based on the dependence of the Seebeck coefficient on the gradient of the density of states (DOS) with energy. Then, given that very sharp DOS would be found in quantum confined structures, the Seebeck coefficient would be greatly enhanced. Other approaches to obtain higher Seebeck coefficients are electron energy filtering [55], which proposes the filtering of the electrons with the lowest mean energy, and resonant scattering [56] by introducing distortions into the DOS. In the case of the electrical conductivity, modulation doping has been used to improve carrier mobility [57]. Also, controlling the crystal orientation or composite engineering has shown results in this sense [58]. The main problem is that an increase in the Seebeck coefficient comes along with a decrease in electrical conductivity, as it is the case in energy filtering.

http://dx.doi.org/10.5772/67730

Therefore, other routes to obtain both an increase in the Seebeck coefficient and electrical conductivity have been proposed, such as band engineering [59], and electron energy filtering are nowadays under study. A recent review on all these strategies can be found in Ref. [58].

The other mentioned route to improving the thermoelectric performance is to engineering the structure of the material to reduce lattice thermal conductivity, what is called phononics engineering [60–62]. This last approach can be understood if one takes into account that classical thermoelectric materials are usually semiconductors. Indeed, for metals, κ is dominated by free electrons, whereas in semimetals and heavily doped semiconductors, both κ_L (lattice thermal conductivity) and κ_e (electron thermal conductivity) play an important role in the total thermal conductivity. In particular, in the case of semiconductors, heat is conducted primarily by the acoustic phonons [51, 52, 63]. Undoubtedly, in recent years, there has been an explosion in the research and understanding of the tailoring of thermal conductivity through nanostructure fabrication [51, 52, 64]. In these cases, low thermal conductivity can be achieved by inhibiting the transport of heat through the lattice vibrations, which are called phonons. Phonons can be divided into those having low, medium, or long wavelengths. **Figure 4** depicts how the nano-inclusions, defects, or vacancies significantly reduce the mean free path of the different phonons, thereby reducing the lattice thermal conductivity [64, 65]. In pure materials (non-alloys or doped), the dominant phonon scattering mechanisms go from boundary scattering to phonon-phonon Umklapp scattering with increasing temperature. Then, in order to reduce the thermal conductivity, point inhomogeneities are usually introduced, such as alloy atoms, dopants, isotope variations, rattlers, and point defects. Through these mechanisms, not only phonons, but also electrons are scattered, and thus, the κ is reduced [51, 52, 62, 66]. In the case of nanostructure fabrication, the idea is to form structures with smaller sizes than the phonon mean free paths, but greater than the electron or hole mean free paths, given that phonons are more strongly scattered by the interfaces than are electrons or holes [67], giving

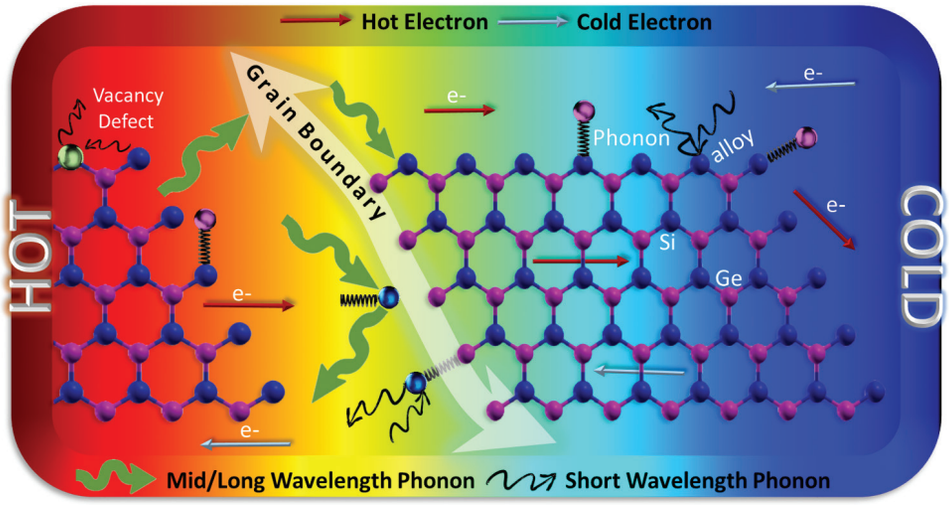

Figure 4. Scheme of the most used strategies for reducing thermal conductivity and their effect on phonon scattering. Grain boundaries scatter mid-long wavelength phonons at their interfaces, while alloy atoms, dopants, defects, lattice vibrations, and nano-inclusions scatter short-wavelength phonons. The electrons, which are depicted as arrows in the figure, are supposedly not scattered and thus electrical conductivity is not altered.

rise to phonon glass-electron crystals (PGEC). As it was said before, the lower the thermal conductivity is, the higher and longer the temperature gradient is maintained and thus more efficient the material results.

3. Thermoelectric properties of silicon-germanium alloys

Silicon-germanium alloys (SiGe) have played a primary role in thermoelectricity in the last decades, although its potential for thermoelectric application was first shown in the 1950s [68–70]. Less than 10 years later, in 1964, a study on how to improve silicon-rich SiGe alloys was published [71, 72], and, the next year, they were used for the first time in a spatial mission from NASA (the SNAP-10 [71]). From that moment onward, they have been successfully used in radioisotope thermoelectric generators (RTGs) for deep-space NASA missions. Bulk silicon-germanium nanostructures (that is, compacted nanograins) are used in the RTGs that power different spacecraft's such as Voyager 1, Voyager 2, Galileo, Ulysses, Cassini, and New Horizons missions [25, 26, 73]. For instance, missions Voyager and Cassini spacecrafts are equipped with RTGs that use a pellet of $^{238}PuO_2$ as the thermal energy source and SiGe as the thermoelectric conversion material. In addition to having very attractive thermoelectric and physical properties, SiGe devices can operate at temperatures up to about 1050°C without significant degradation [25, 73]. For high-temperature applications (above 600°C), SiGe alloys have a high thermoelectric efficiency and have been the type of conduction and the carrier concentration in SiGe can be controlled by doping with phosphorous (*n*-type) or boron (*p*-type). As a consequence, a total of 28 USA space missions have safely flown powered by RTGs [26, 73]. In this field, SiGe used as thermoelectric conversion material has accumulated over 250 million devices working hours in space applications (running for over 40 years in Voyager missions) without failure [25, 26, 74].

In all these years, different studies on how to increase the efficiency of these materials, such as the use of grain-refined alloys [75, 76], nano-inclusions [77], SiGe superlattices fabrication [78], and understanding how the grain size affects thermal conductivity [79], were performed. Also, novel methods for the fabrication of SiGe, such as the chill casting method [80], milling and sintering techniques [81], high-energy ball milling [82], spark plasma sintering [83, 84], and mechanical alloying, were developed. The improvements achieved in SiGe were all related to nanostructuring the material and reducing the lattice thermal conductivity. In 2008, a theoretical work proposed that the introduction of silicide nanoparticles into the SiGe matrix would reduce drastically the thermal conductivity [85]. That is, if the grain size is smaller than the mean free path of the phonons, the total effect is a reduction in the effective mean free path and thus a reduction in the thermal conductivity. Another route studied has been the enhancement of the power factor in SiGe through the concept modulation doping [86]. In this case, a 40% power factor enhancement in $Si_{80}Ge_{20}$ bulk nanocomposites has been reported, and it was a direct result of the enhanced mobility due to this modulated doping [86]. With all these advances, zT values for nanostructured bulk SiGe as high as 1.3 for *n*-type and 0.95 for *p*-type have been measured [87–89].

Apart from these successes in the increase of thermoelectric efficiency and the space applications of SiGe, there is another outstanding property that makes SiGe appealing for many

http://dx.doi.org/10.5772/67730

other applications, which is the possibility of integration (compatibility) in the technology of semiconductors based on silicon. This can be made through thin films fabrication of SiGe on silicon like it is done in the complementary metal-oxide semiconductors (CMOS) industry [90]. In general, thermoelectricity struggles with the lack of cheap, abundant, and environmentally friendly materials. Recent works have emphasized the importance of considering the relationship between material's price, manufacturing costs, and efficiency to consider different thermoelectric materials [91]. Silicon-germanium could overcome this deficiency by proposing high harvested power density, abundant on earth, low toxicity, and cost-efficiency. These characteristics increase the interest of SiGe among other thermoelectric materials [90, 91].

3.1. Some strategies for reducing the thermal conductivity of silicon-germanium

The challenge of obtaining ultra-low thermal conductivities in silicon-germanium, in particular, for thermoelectric applications, is not recent. **Figure 5** represents the different strategies that have been followed to fabricate nanostructures with reduced thermal conductivity in SiGe.

In the case of pure silicon and germanium, measurements in bulk, the room temperature thermal conductivities are ~140 W K^{-1} m^{-1} [67] and ~60 W K^{-1} m^{-1}, respectively [30]. However, SiGe alloys provide a significant reduction in thermal conductivity versus the above-mentioned values. Depending on the germanium content, values ranging from ~20 to ~9 W K^{-1} m^{-1} have been measured in bulk [30]. The lowest value of room temperature thermal conductivity has been achieved for a stoichiometry of $Si_{0.8}Ge_{0.2}$ (~9 W K^{-1} m^{-1}), which is still large for thermoelectric applications. Nevertheless, an even lower value (<1 W K^{-1} m^{-1}) has been measured for films grown by sputtering with a $Si_{0.8}Ge_{0.2}$ stoichiometry [92]. The difference with the previous case is that these films were grown through metal-induced crystallization (MIC),

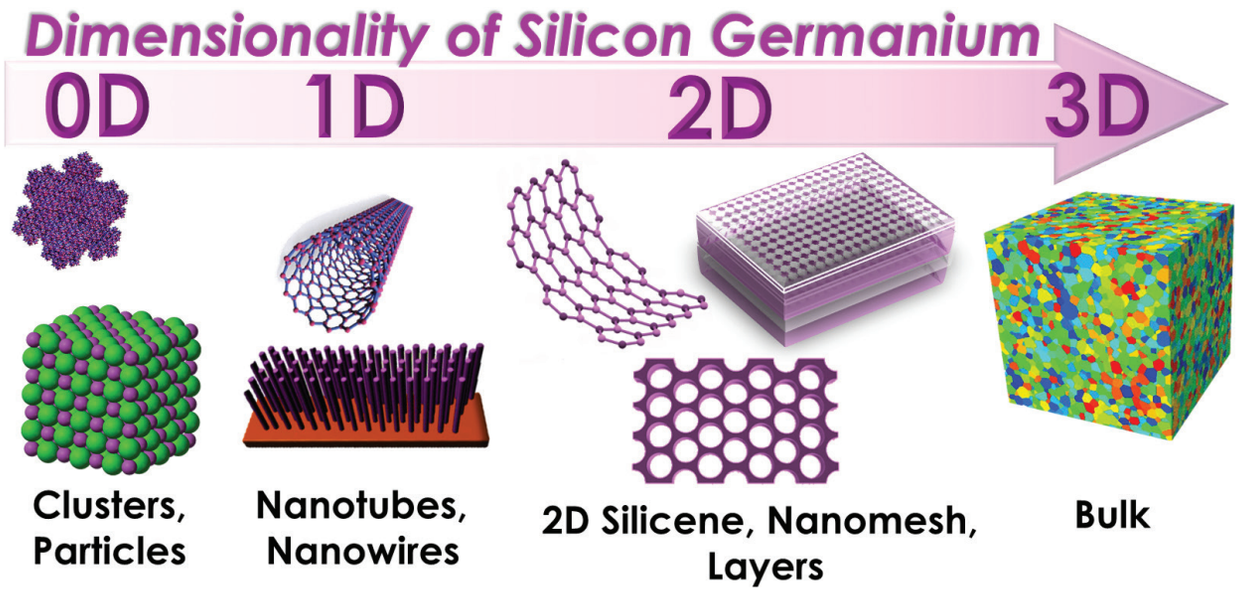

Figure 5. One of the strategies that has been proven to be useful in improving thermoelectric performance is to reduce dimensionality. Here, different configurations that the silicon-germanium has been fabricated at the nanometric scale to improve its thermoelectric properties are shown.

which allows the reduction of the crystallization temperature of the SiGe. With this technique, films with thermal conductivity values down to ~1.2 W K^{-1} m^{-1} at room temperature [92, 93] have been obtained. (See Section 4 for more details.)

At the same time, the growing interest in 2D materials has also triggered the study of 2D silicene [94], which has low thermal conductivity and high power factor. Although the thermal conductivity of silicene has not been measured experimentally due to the difficulty of synthesizing freestanding silicene (and also the complication to carry out thermal measurements in the in-plane direction), several numerical simulations have predicted a thermal conductivity of silicene at room temperature from 5 to 70 W K^{-1} m^{-1} [94–97]. Also graded $Si_{1-x}Ge_x$/Si superlattice structures have been theoretically proposed and fabricated. The idea behind these structures was to demonstrate a thermal rectification effect derived from a theoretical model (the kinetic collective model), which showed that the thermal boundary resistance of a $Si_{1-x}Ge_x$/Si depends on the direction of the heat flow if the structure is symmetric. The predicted effect would cause around 40% difference depending on the heat flow direction. Experimentally, these graded superlattices were fabricated via molecular beam epitaxy (MBE) on silicon substrates, and further studies on the impact of the composition, strain, or alloy inhomogeneities [98] showed that the transport properties could be engineered, obtaining values for the thermal conductivity as low as 2.2 W m^{-1} K^{-1} [99].

Another 2D structure that has recently been developed is the fabrication of nanomeshes (nanoporous or holey silicon or SiGe membranes). These structures can be fabricated by sputtering deposition in large areas [100], which offers the advantages of scalability and flexibility required for real applications [100–102]. Moreover, the variation of the geometry of the mesh influences its thermal conductivity [100, 102], allowing a further control on this parameter. In particular, the thermal conductivity of the nanomeshes was reduced as the diameter of the pores became smaller, achieving values that varied from $\kappa = 1.54 \pm 0.27$ W K^{-1} m^{-1}, down to the ultra-low $\kappa = 0.55 \pm 0.10$ W K^{-1} m^{-1} value [100]. The latter is well below the amorphous limit, while the Seebeck coefficient and electrical conductivity of the material were retained [100]. (More details of these nanomeshed structures will be given in Section 5.)

In addition to phonon transport engineering [59, 60], different technological strategies such as the fabrication multilayers [103] and channels with reduced dimensionality such as 1D nanotubes [104] and 1D nanowires [105] have achieved a significant reduction in the thermal conductivity. Furthermore, several authors have demonstrated that the obvious reduction in cross-plane thermal conductivity in SiGe 0D cluster—particle (quantum dots) [106] superlattices is primarily due to the increased physical roughness at the superlattice interfaces and not due to quantum confinement effects [107, 108].

Figure 6 summarizes the current state of the art for silicon-germanium in terms of thermoelectric properties. Here, the most promising materials in the form of bulk, thin films, nanomeshes, nanowires, and nanotubes are shown. It is worth noting in these figures that the results of our works, which will be explained later, namely the MIC films and the nanomeshes, are among the best-performing materials. In terms of Seebeck coefficient

http://dx.doi.org/10.5772/67730

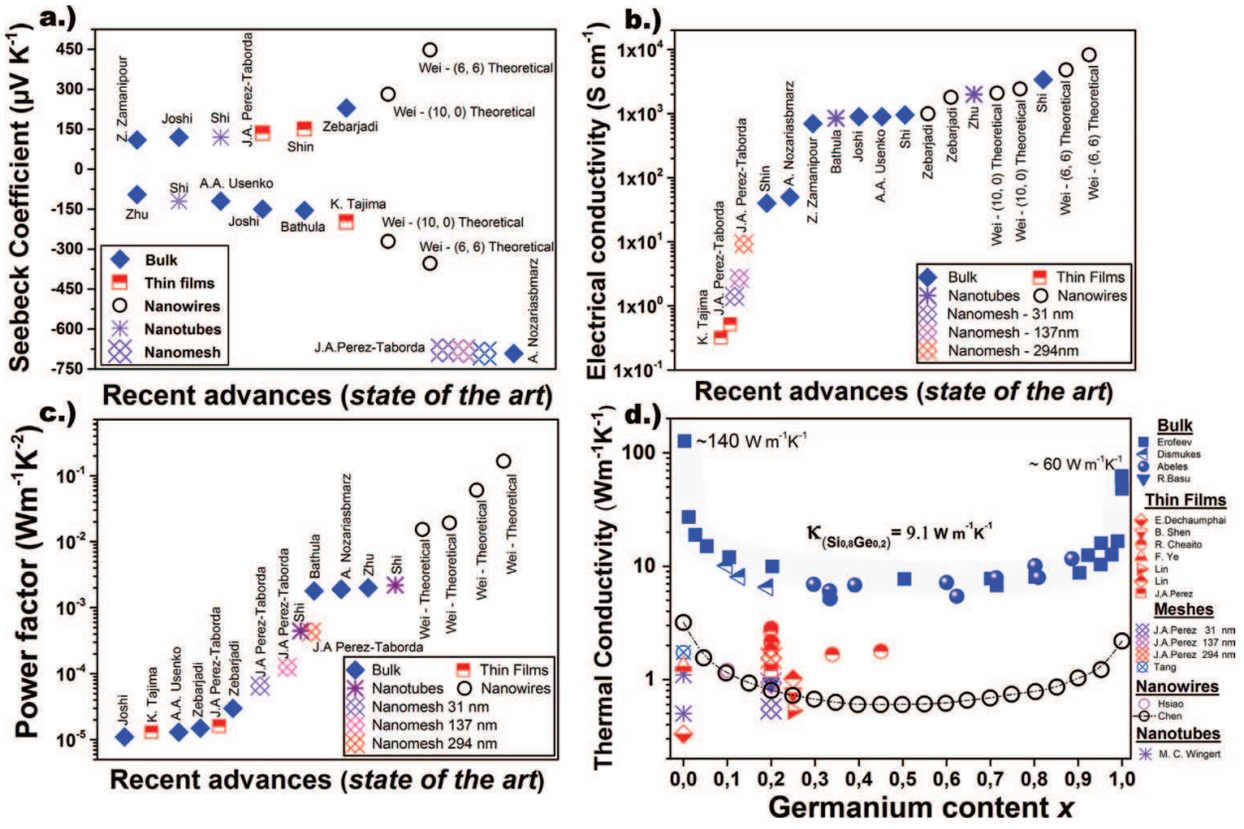

Figure 6. A summary of the latest reported measurements of different structures of Si_xGe_{1-x} is presented, shows (a) Seebeck coefficient, (b) electrical conductivity, and (c) power factor reported for bulk, thin films, nanomeshes, nanowires, and nanotubes. (d) The thermal conductivity for different Si_xGe_{1-x} nanostructures and bulk samples as a function of the alloy composition. This figure is adapted from Ref. [100].

(see **Figure 6a**), the values measured for MIC SiGe thin films are comparable to other values measured in different thin films fabricated with other techniques, while the nanomeshes present the highest Seebeck coefficients, only comparable to values measured in bulk. Nevertheless, the values of electrical conductivity (**Figure 6b**) are quite low, when compared to the values of bulk or nanotubes, but in the order or even better than the values given for thin films. The enhancement of the electrical conductivity within those structures is one of the improvements that are being studied nowadays.

On a whole, the power factor (presented in **Figure 6c**), which takes into account the square of the Seebeck coefficient times the electrical conductivity, shows that the MIC films have power factors compared to other thin films (even higher) and the values achieved in nanomeshes are only overridden by bulk materials and nanotubes [109] (note that the black circles are theoretical calculations, not actual measurements). The last data show the thermal conductivity of different alloy compositions for different kinds of structures (**Figure 6d**). Here, it is worth noting that the values measured for both MIC films and nanomeshes are well below the values measured for crystalline bulk SiGe and among the lowest ever recorded, comparable with the value of the amorphous material (which is 1 W m^{-1} K^{-1}).

4. Thin films: improvement of the thermoelectric performance through the reduction of thermal conductivity of nanocrystalline $Si_{0.8}Ge_{0.2}$ films by sputtering deposition

Silicon-germanium thin films can be easily *p*- or *n*-type doped at room temperature when the material is amorphous. Nevertheless, doping is particularly difficult when the material is crystalline, given that it is usually crystallized at high temperatures. Si_xGe_{1-x} films grown by different techniques, such as low-pressure chemical vapor deposition (LPCVD) or sputtering, turn out to be amorphous unless the deposition itself is performed at very high temperatures [110–112]. Certainly, amorphous SiGe layers are not an option to be used as thermoelectric materials, given their low Seebeck and low electrical conductivity. Therefore, the main challenge with these Si_xGe_{1-x} alloys, which are to be applied in large-scale practical applications, has not yet been overcome due to the difficulties in the growth of high-quality, highly crystalline, low-cost, and appropriately doped films. On that sense, some examples that can be found in the literature obtained in our lab are compiled in this section.

Recently, metal-induced crystallization (MIC) [92, 113, 114] has proved to be an interesting alternative to reduce the crystallization temperature required for SiGe. This process is based on the growth of the films on substrates with Au [115], Ag [116], Al [117], Ni [118], Cr [119], or Sn [120] layer. Then, an appropriate heat treatment is performed, allowing the gold from the film to migrate through the semiconductor film all the ways to the surface. This gives rise to a eutectic mixture. The Au-Si eutectic temperature occurs around 350°C, Au-Ge being at around 361°C [121]. Using this MIC technique, quite promising results have been reported recently for thin films of boron-doped $Si_{0.8}Ge_{0.2}$ (*n*-type) grown by sputtering, resulting in films with a good power factor and a very low thermal conductivity [92]. In that work, two different approaches were followed: (i) *in situ* MIC (depositing the films at different controlled temperatures during the sputtering process) and (ii) *ex situ* MIC (deposition of the films at room temperature in the sputtering chamber and subsequently post-annealing in an external furnace under a controlled atmosphere) [92].

The structural evolution from amorphous to crystalline as a function of the different treatment temperatures can be observed in **Figure 7** through the Raman spectra, both for *in situ* (left hand, red color) and *ex situ* (right hand, blue color) MIC films for different temperatures. It can be seen that the vibration modes appear as broad bands for room temperature treatments (see **Figure 7a** and **e**), which means that the material is amorphous. Then, the peaks become narrower as the treatment temperatures increase. Moreover, the Si-Si vibrational peak shows a clear red shift for the highest temperature (500°C) of the *ex situ* samples (**Figure 7d**). This shift may be related to the formation of silicon-rich clusters. Moreover, the relative intensities and frequencies corresponding to the main peaks present in the Raman spectra are strongly dependent on the alloy composition.

A closer look at the Si-Si peak reveals that it is, in fact, a convolution of two peaks; a very narrow peak corresponding to the Raman spectrum of crystalline silicon-rich SiGe and a broader, smaller peak corresponding to the Si-Si vibrations are typically found in $Si_{0.8}Ge_{0.2}$. This could be an indication that silicon is partially segregated in the *ex situ* samples. The peaks observed in the *in situ* samples are narrower than those of the *ex situ* annealed samples, which confirms the high

http://dx.doi.org/10.5772/67730

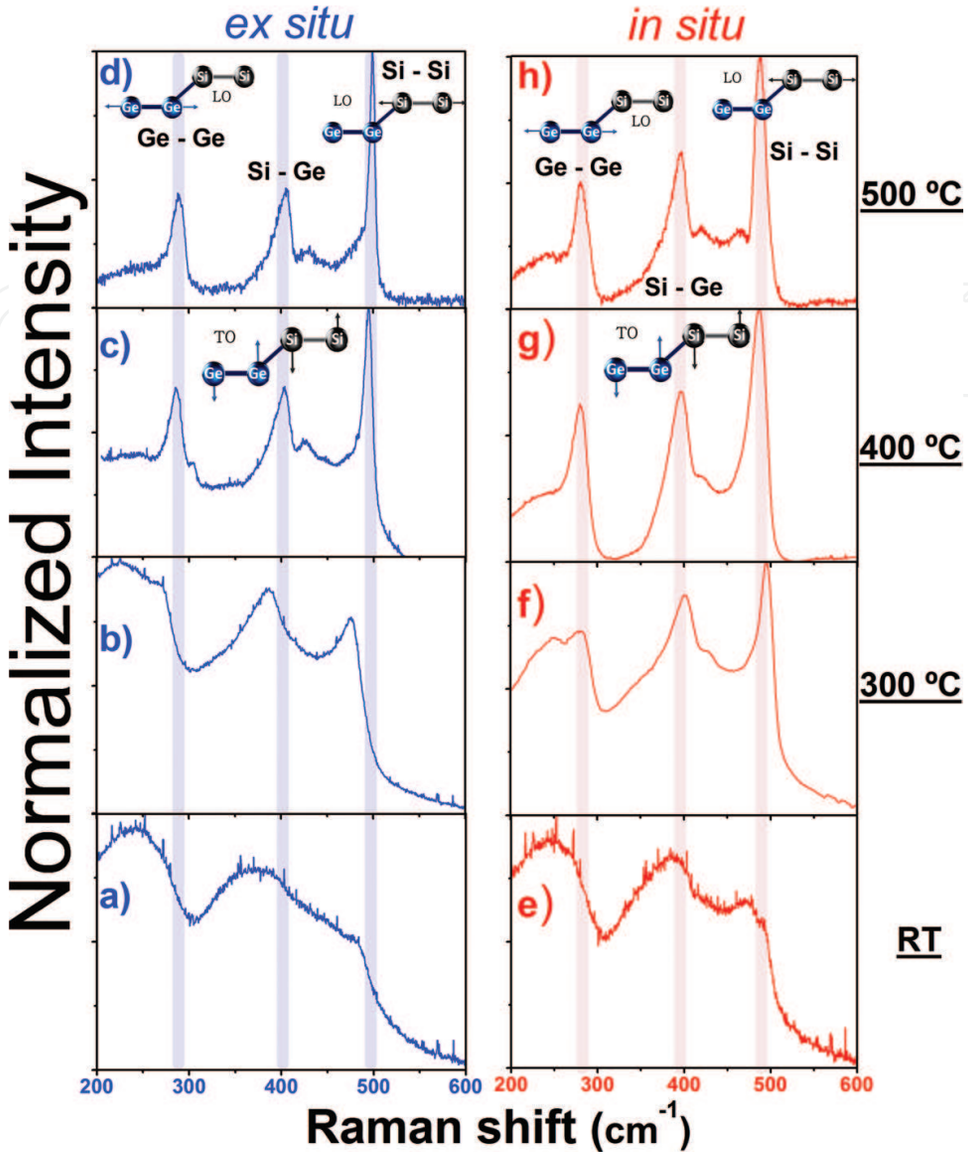

Figure 7. Raman spectra of thin films deposited on gold/glass substrates: *ex situ* thermal treatment (in blue: a, b, c, and d) and *in situ* thermal treatment (in red: e, f, g, and h) for samples treated at RT, 300, 400, and 500°C, respectively. The expected vibrational bands (schematically represented) corresponding to Ge-Ge, Si-Si, and Si-Ge bonds are marked on the figure. With permission from Ref. [92].

degree of crystalline order. Furthermore, these results clearly indicate that whereas, in the *in situ* treatment, the crystallization starts at 300°C, the crystallization onset is lower for *ex situ* treatments. It is interesting to note that in the 400–500 cm^{-1} region, secondary modes start to appear at high temperatures. These modes might be associated with the formation of a compositional gradient due to segregation of Si and Ge, which promotes predominantly Si cluster formation. These clusters would remain embedded in the SiGe matrix when the post-annealing is performed.

Then, the structural analysis by synchrotron radiation-grazing incidence X-ray diffraction (SR-GIXRD) for samples treated at 500°C is shown in **Figure 8**. In order to perform the XRD study, the gold layer was also selectively removed by potassium iodide etching. Nevertheless, gold diffraction maxima are dominant in the *ex situ* treated sample, which means that not all the gold was removed. This indicates that the gold, instead of migrating completely to the

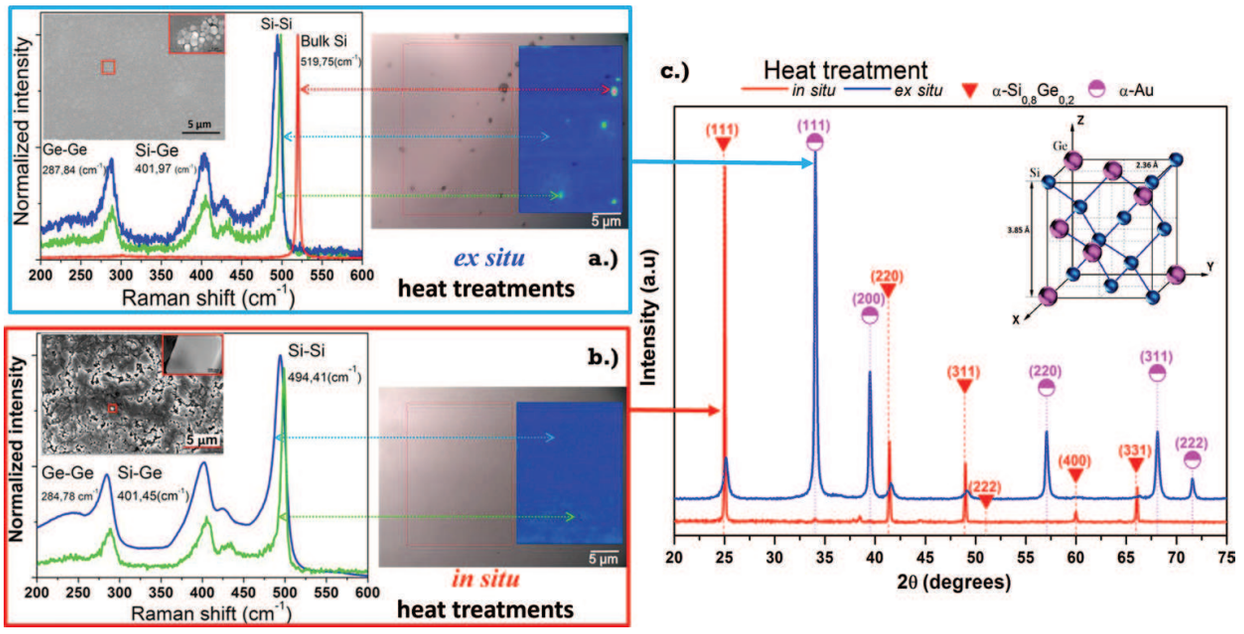

Figure 8. (a) and (b) present different measurements for the *ex situ* (a) and *in situ* (b) MIC fabricated films with 500°C treatment temperatures. On the right side, the optical image of the surface along with a Raman mapping of the surface is presented. In the left side, the different Raman spectra collected corresponding to $Si_{0.8}Ge_{0.2}$ (blue color), nano-$Si_{1-x}Ge_x$ (green color), and pure silicon (red color) are shown (note that for the *in situ* film, b), there is no evidence of silicon segregation). The inset at the left side presents SEM image of the film surface. (c) Synchrotron radiation SR-GIXRD diffractograms measured at 1.3775 Å wavelength for *ex situ* (blue color) and *in situ* (red color) MIC fabricated films, with heat treatments at 500°C. The heights of the intensities in dotted lines correspond to the Si-Ge phase intensity values given in the JCPDS 04-016-6750 data sheet. The inset shows the calculated lattice parameters for the Si-Ge films. This figure is adapted from Ref. [92].

surface during the *ex situ* MIC treatment, part of it stayed, trapped inside the film. In the case of samples deposited *in situ* at temperatures of 500°C, the diffraction peak intensities at (111), located at 2θ=25.33° for the synchrotron radiation source, are higher than the intensities of samples treated *ex situ*.

The low values of thermal conductivities (1.13 and 1.23 W m^{-1} K^{-1} for *in situ* and *ex situ* thermal treated at 500°C, respectively) obtained in Ref. [92] have been associated with the formation of Si-rich SiGe and Si clusters during the gold-induced crystallization, which creates plenty of phonon scattering sites at the grain boundaries. The best power factors were achieved for samples grown at 500°C, that is, *in situ* MIC. The results indicate a maximum of 16 μW m^{-1} K^{-2} at 315°C, which is the best-reported value, to date, for SiGe films grown by DC sputtering with Au-MIC—similar to the state-of-the-art values available in the literature for Si-Ge bulk samples. This is due to the fact that this sample is not contaminated with gold and also that the doping has not been lost by this thermal treatment.

In the same way, these results also suggest two different mechanisms of induced crystallization dependent on the type of heat treatment (*ex situ* and *in situ* MIC). For the *ex situ* samples, the gold layer travels through the Si-Ge film grown at RT when heated afterward at 500°C, while in the case of *in situ* treatment, a eutectic is formed and the nanocrystalline Si-Ge film seems to be formed underneath.

http://dx.doi.org/10.5772/67730

5. Nanomeshes: record low thermal conductivities in large-area nanoporous $Si_{0.8}Ge_{0.2}$ for enhanced thermoelectric applications

Another recent example of a reduction in thermal conductivity by using the low-dimensional concept has been recently reported [100]. These large-area nanomeshed films were fabricated by DC sputtering of $Si_{0.8}Ge_{0.2}$ on highly ordered porous alumina matrices (see **Figure 9a**), in such a way that the formed $Si_{0.8}Ge_{0.2}$ film replicated the porous alumina structure, resulting in the nanomeshed films shown in **Figure 9b**. A very good control of the nanomesh geometrical features (pore diameter, pitch, and neck) was achieved thanks to the alumina templates used, with pore diameters ranging from 294 ± 5 nm down to 31 ± 4 nm. The method developed is able to provide large areas of nanomeshes in a straightforward and reproducible way, being easily scalable for industrial applications.

Most importantly, as shown in **Figure 10a**, the thermal conductivity of the films was reduced as the diameter of the porous became smaller, achieving values that varied from $\kappa = 1.54 \pm 0.27$ W K^{-1} m^{-1}, down to the record low $\kappa = 0.55 \pm 0.10$ W K^{-1} m^{-1} value. The latter is well below the amorphous limit, while both the Seebeck coefficient and electrical conductivity of the material were maintained (see **Figure 10b**).

Likewise, as in the previous case for the nanocrystalline $Si_{0.8}Ge_{0.2}$ films grown by sputtering deposition, the nanomeshed SiGe films were oriented along the [111] direction, as revealed by XRD measurements (see **Figure 11a**). Raman spectra showed the three characteristic

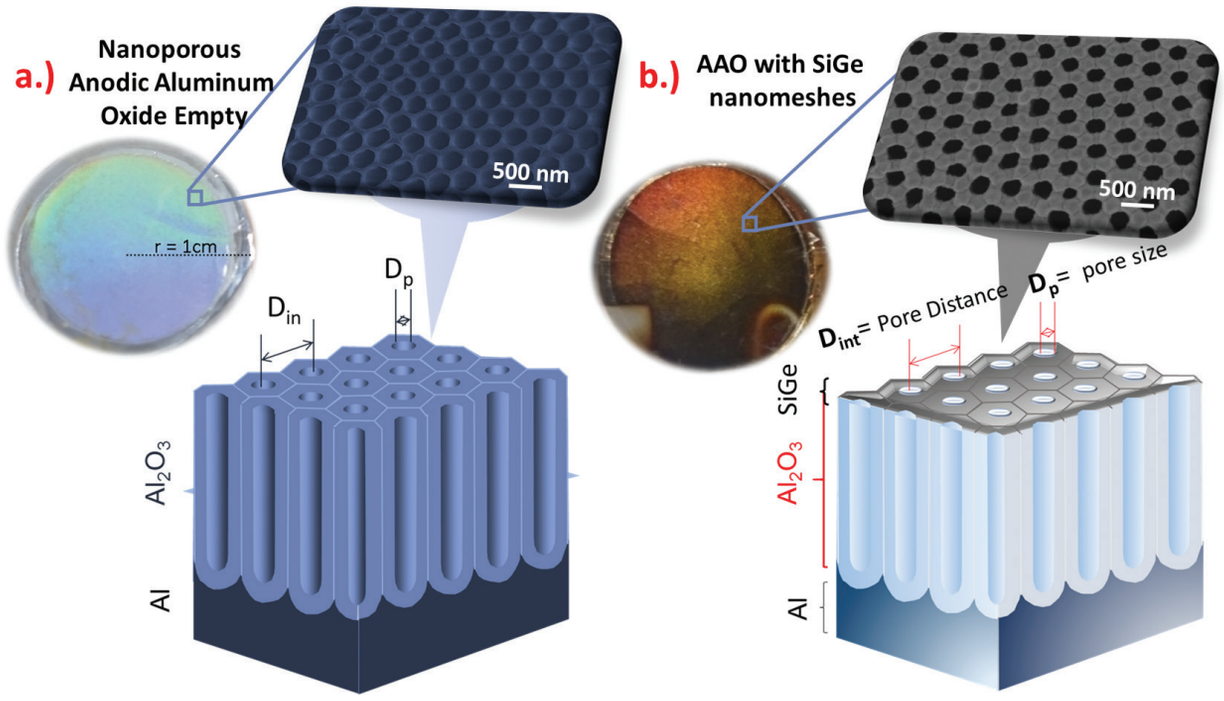

Figure 9. (a) Sketch and optical image of a porous alumina template and (b) the SiGe film nanomesh fabricated on top of it.

vibrational modes obtained for polycrystalline SiGe (see **Figure 11b**) and showed a homogenous phase in all the film.

Additionally, the chemical/surface potential of the $Si_{0.8}Ge_{0.2}$ nanomeshed films was studied by Kelvin probe microscopy (KPM). **Figure 12a** and **b** shows the SEM image and the AFM surface topography of a 294 ± 5 nm porous size nanomeshed film, which presents a homogeneous profile of the surface potential (see **Figure 12c**). This indicates that the work function of the films is homogeneous, confirming the homogeneity in the chemical composition obtained by Raman, and no potential drop is observed at the grain boundaries.

On the one hand, as far as the thermal conductivity is concerned, it is highly reduced when compared to bulk or thin films. This reduction is due to alloying, phonon boundary scattering on the upper/lower boundaries, and crystallite boundaries within the nanomeshes. Moreover, the measurements showed that the smaller the pore diameter is, the larger the thermal conductivity reduction in the $Si_{0.8}Ge_{0.2}$ nanomesh. This can be understood as a result of the enhanced scattering on the pore boundaries, along with the higher disorder or even coherent phonon effects that could be playing a role in the nanomeshed structures, when compared to plain films. Using this approach, it is possible to control thermal transport of these films

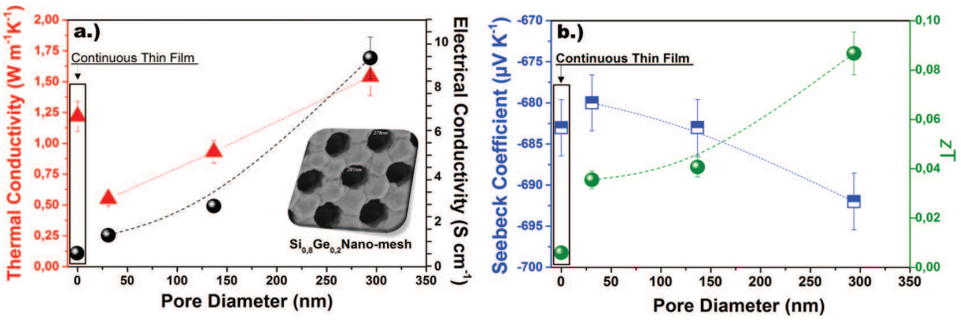

Figure 10. (a) Thermal conductivity (κ, red triangles) and electrical conductivity (σ, black spheres) and (b) Seebeck coefficient (S, blue squares) and figure of merit (zT, green spheres) plotted versus the pore diameter of the nanomesh. The transport properties obtained for a $Si_{0.8}Ge_{0.2}$ film grown under the same conditions are also plotted for comparison (inside the rectangle on the left of each graph, corresponding to continuous thin film). This figure is adapted from Ref. [100].

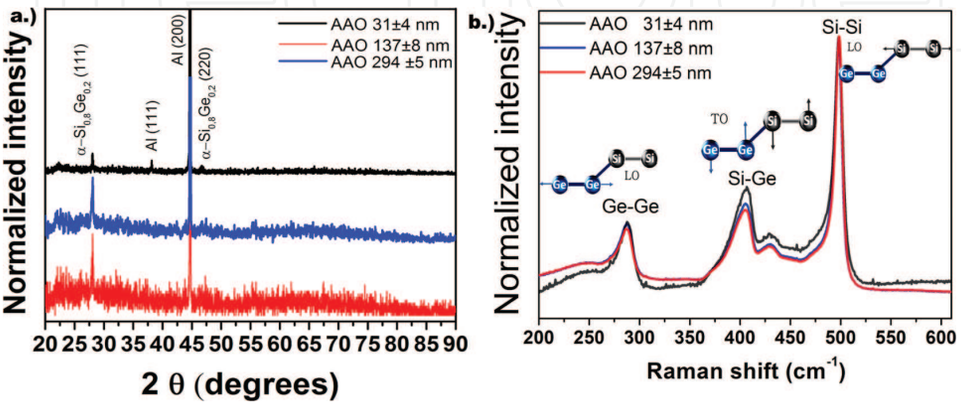

Figure 11. (a) X-ray diffraction and (b) Raman spectra of a $Si_{0.8}Ge_{0.2}$ grown on nanomeshes with a pore diameter of 31 nm (black line) 137 nm (blue line) and 294 nm (red line). This figure is adapted from Ref. [100].

http://dx.doi.org/10.5772/67730

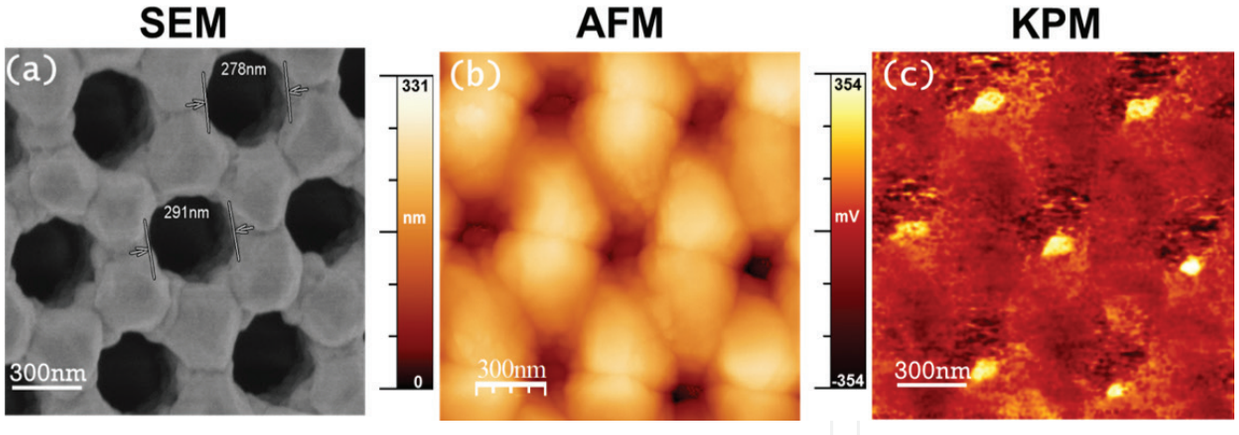

Figure 12. (a) SEM image of a $Si_{0.8}Ge_{0.2}$ nanomeshed film of 294 ± 5 nm pore size. (b) Topography image by AFM and (c) surface potential image by KPM. The uniformity in the contrast of the KPM image reveals homogeneity in the surface potential of the film. This figure is adapted from Ref. [100].

through nano-engineering. Moreover, the power factors of the nanomeshes are higher in the structures with larger pores (and larger distances between the pores), and consequently, they are found smaller in the more disordered structures, which comprise denser pore structure and smaller pore diameters.

The power factors are found to be between 65 and 455 $\mu W\,K^{-2}\,m^{-1}$, which seem to be as large as some of the last reported values for bulk $Si_{0.8}Ge_{0.2}$. This is attributed to the fact that the electrical conductivity in the nanomeshes with large interpore distance is much larger than the more dense nanomeshes, whereas the Seebeck coefficient remains almost the same [100]. while still retaining reasonable power factors, which opens the door for efficient thermoelectric applications for this alloy.

6. Concluding remarks and future directions

In summary, this chapter has shown how the nanostructuration of SiGe takes advantage of the reduction in the lattice thermal conductivity while maintaining the thermoelectric properties of the material, which makes the material quite competitive with others conventionally used. Moreover, the two examples of nanostructuration that have been described here in more detail, namely the sputtered MIC films and the nanomeshes present several advantages over other techniques, such as the possibility of coating large areas thanks to the sputtering process, which is also industrially scalable. Furthermore, the sputtering onto alumina templates, which gives rise to the nanomeshes, can also cover large areas, given that the aluminum oxide templates can be fabricated over large-area aluminum substrates. In the case of nanomeshes, the drastic reduction in the thermal conductivity achieved is due to alloying, phonon boundary scattering on the upper/lower boundaries, and crystallite boundaries. Therefore, this makes the method cost-effective to be scaled into the industry. Another key thing to remember is that both nanostructures (MIC films and nanomeshes) are compatible with silicon technology, opening the door to applications in electronic devices, which need to have thermal dissipation. This provides not only a novel approach to growing this kind of

structures in a simple and reliable way, but also an important route toward achieving high conversion efficiency and highly scalable thermoelectric materials.

This chapter presents the most recent advancements in SiGe alloys for its use as efficient thermoelectric material. To this end, it is important to understand the mechanisms that govern the thermal conductivity, in order to engineer the material to reduce it as much as possible without affecting other thermoelectric properties. The thriving expansion of new capabilities of 1D and two-dimensional SiGe has progressed rapidly during the last few years. Although most of the two-dimensional materials have a simple honeycomb lattice structure, understanding the phonon transport mechanism in such atomic thin SiGe seems not an easy task. It is obviously important to recognize that no single technology can meet the world's energy needs in the twenty-first century; one needs a combination of many technologies in which the thermoelectric materials can undoutebtedly play a role. Further, these large-area films or nanomeshes provide a novel approach to growing nanostructured thermoelectric materials in a simple and reliable way.

Author details

Jaime Andrés Pérez-Taborda, Olga Caballero-Calero and Marisol Martín-González*

*Address all correspondence to: marisol@imm.cnm.csic.es

IMM-Instituto de Microelectrónica de Madrid (CNM-CSIC), Madrid, Spain

References

[1] D.C. Brock (Ed.), Moore's law at forty. *Understanding Moore's law: four decades of innovation*, Chemical Heritage Foundation (2006) last access: https://issuu.com/chemheritage/docs/understanding-moores-law?e=1220

[2] M. Martín-González, O. Caballero-Calero, P. Díaz-Chao, Renewable and Sustainable Energy Reviews **24**, 288 (2013).

[3] J. Conti, International energy outlook 2016 Report No. DOE/EIA-0484 US Energy Information Administration (eia), Washington DC (2016).

[4] P. Fragkos, N. Tasios, L. Paroussos, P. Capros, S. Tsani, Energy Policy **100**, 216 (2017).

[5] Communication from the Commission to the European Parliament, The Council. The Road from Paris: assessing the implications of the Paris Agreement and accompanying the proposal for a Council decision on the signing, on behalf of the European Union, of the Paris agreement adopted under the United Nations Framework Convention on Climate Change. European Commission, Brussels, 2.3.2016 COM(2016) 110 final last access: https://ec.europa.eu/transparency/regdoc/rep/1/2016/EN/1-2016-110-EN-F1-1.PDF

[6] B. Obama, The irreversible momentum of Clean energy, Science 355 (January (6321)) (2017) 126–129

[7] H. Theuerer, J. Kleimack, H. Loar, H. Christensen, Proceedings of the Institute of Radio Engineers **48**, 1642 (1960).

[8] P. Balk, Journal of the Electrochemical Society **118**, 494 (1971).

[9] H. Daembkes, H.-J. Herzog, H. Jorke, H. Kibbel, E. Kasper, IEEE Transactions on Electron Devices **33**, 633 (1986).

[10] T. Pearsall, J. C. Bean, IEEE Electron Device Letters **7**, 308 (1986).

[11] H. Temkin, T. Pearsall, J. Bean, R. Logan, S. Luryi, Applied Physics Letters **48**, 963 (1986).

[12] G. L. Patton, S. S. Iyer, S. Delage, S. Tiwari, J. Stork, IEEE Electron Device Letters **9**, 165 (1988).

[13] H. Liu, D. Landheer, M. Buchanan, D. Houghton, Applied Physics Letters **52**, 1809 (1988).

[14] R. Taft, J. D. Plummer, S. Iyer, IEEE Electron Device Letters **10**, 14 (1989).

[15] T.-J. King, J. R. Pfiester, J. D. Shott, J. P. McVittie, K. C. Saraswat, in *Electron Devices Meeting, 1990. IEDM'90. Technical Digest., International* (IEEE, 1990), p. 253.

[16] R. Soref, F. Namavar, J. Lorenzo, Optics Letters **15**, 270 (1990).

[17] D. Houghton, J.-P. Noël, N. Rowell, Materials Science and Engineering: B **9**, 237 (1991).

[18] D. Shen, J. Conde, V. Chu, S. Aljishi, J. Z. Liu, S. Wagner, IEEE Electron Device Letters **13**, 5 (1992).

[19] S.-B. Hwang, Y. Fang, K.-H. Chen, C.-R. Liu, J.-D. Hwang, M.-H. Chou, IEEE Transactions on Electron Devices **40**, 721 (1993).

[20] E. Kasper, A. Gruhle, H. Kibbel, *in Electron Devices Meeting, 1993. IEDM'93. Technical Digest., International* (IEEE, 1993), p. 79.

[21] E. Crabbe, B. Meyerson, J. Stork, D. Harame, in *Electron Devices Meeting, 1993. IEDM'93. Technical Digest., International* (IEEE, 1993), p. 83.

[22] S. Jeng et al., IEEE Electron Device Letters **22**, 542 (2001).

[23] J.-S. Rieh et al., in Electron Devices Meeting, 2002. IEDM'02. International (IEEE, 2002), p. 771.

[24] J. D. Cressler, C. Coen, S. Zeinolabedinzadeh, P. Song, R. Schmid, M. Oakley, P. Chakraborty, in *2016 IEEE Compound Semiconductor Integrated Circuit Symposium (CSICS)*2016), p. 1.

[25] R. R. Furlong, E. J. Wahlquist, Nuclear News **42**, 26 (1999).

[26] George R. Schmidt, Robert L. Wiley, Rebecca L. Richardson, and Richard R. Furlong, AIP Conference Proceedings 746, 429 (2005); doi: http://dx.doi.org/10.1063/1.1867159

[27] PATEL, M. R. *Spacecraft Power Systems* CRC-Press, Boca Raton, Florida/USA, 2004. ISBN 0-8493-2768-5.

[28] C. Kelly, in Space Nuclear Power Systems (1987).

[29] G. L. Bennett, C. W. Whitmore, W. R. Amos, "On the Development of the Power Sources for the Ulysses and Galileo Missions", Proceedings of the European Space Power Conference, 1989-October-2-6.

[30] R. Basu et al., Journal of Materials Chemistry A **2**, 6922 (2014).

[31] M. Haras, V. Lacatena, T. M. Bah, S. Didenko, J. F. Robillard, S. Monfray, T. Skotnicki, E. Dubois, IEEE Electron Device Letters **37**, 1358 (2016).

[32] X. Zhang, L.-D. Zhao, Journal of Materiomics **1**, 92 (2015).

[33] Goetberger, Adolf; Knobloch, Joachim; Voss, Bernhard. Crystalline silicon solar cells. editorial John Wiley & Sons Ltd, 1998, vol. 1.

[34] A. Martí, A. Luque, Next Generation Photovoltaics: High Efficiency through Full Spectrum Utilization, edited by A. Martí and A. Luque, Eds.; Institute of Physics, Bristol, 2003.

[35] L.M. Fraas Low-Cost Solar Electric Power Springer International Publishing, Cham (2014) http://dx.doi.org/10.1007/978-3-319-07530-3

[36] U. Rau and T. Kirchartz, in Photon Management in Solar Cell, edited by R. B. Wehrspohn, U. Rau , and A. Gombert (Wiley-VCH, Weinheim, 2015)

[37] M. A. Green, K. Emery, Y. Hishikawa, W. Warta, E. D. Dunlop, Progress in Photovoltaics: Research and Applications **23**, 1 (2015).

[38] Green, M. A., Emery, K., Hishikawa, Y., Warta, W., & Dunlop, E. D. (2015). Solar cell efficiency tables (Version 45). Progress in photovoltaics: research and applications, 23(1), 1–9.

[39] P. J. Reddy, *Solar Power Generation: Technology, New Concepts & Policy* (CRC Press, 2012).

[40] G. Carr, The Economist **11**, 21 (2012).

[41] D. M. Powell, M. T. Winkler, H. Choi, C. B. Simmons, D. B. Needleman, T. Buonassisi, Energy & Environmental Science **5**, 5874 (2012).

[42] D. Feldman et al., Photovoltaic System Pricing Trends: Historical Recent Near-Term Projections 2013 Edition, Oak Ridge, TN, USA:U.S. Dept. Energy, 2013.

[43] M. P. Paranthaman, W. Wong-Ng, R. N. Bhattacharya, *Semiconductor materials for solar photovoltaic cells* (Springer, 2015), Vol. 218.

[44] R. Keyes, IBM Journal of Research and Development **32**, 84 (1988).

[45] P. S. Peercy, Nature **406**, 1023 (2000).

[46] M. Ieong, B. Doris, J. Kedzierski, K. Rim, M. Yang, Science **306**, 2057 (2004).

[47] T. Ihn, *Semiconductor Nanostructures: Quantum States and Electronic Transport* (Oxford University Press, 2010).

[48] Y. Nishi, R. Doering, *Handbook of Semiconductor Manufacturing Technology* (CRC Press, 2000).

[49] J. Cressler, *in SiGe and Si Strained-Layer Epitaxy for Silicon Heterostructure Devices* (CRC Press, 2007).

[50] W. G. Zeier, J. Schmitt, G. Hautier, U. Aydemir, Z. M. Gibbs, C. Felser, G. J. Snyder, Nature Reviews Materials **1**, 16032 (2016).

[51] E. S. Toberer, L. L. Baranowski, C. Dames, Annual Review of Materials Research **42**, 179 (2012).

[52] A. Shakouri, Materials Research **41**, 399 (2011).

[53] A. Moure, M. Rull-Bravo, B. Abad, A. Del Campo, M. M. Rojo, M. H. Aguirre, A. Jacquot, J. F. Fernandez, M. Martin-Gonzalez, Nano Energy **31**, 393 (2017).

[54] L. Hicks, M. Dresselhaus, Physical Review B **47**, 12727 (1993).

[55] D. Vashaee, A. Shakouri, Physical Review Letters **92**, 106103 (2004).

[56] J. P. Heremans, V. Jovovic, E. S. Toberer, A. Saramat, K. Kurosaki, A. Charoenphakdee, S. Yamanaka, G. J. Snyder, Science **321**, 554 (2008).

[57] Q. Hou, B. Gu, Y. Chen, Y. He, J. Sun, Applied Physics A **114**, 943 (2014).

[58] A. M. Dehkordi, M. Zebarjadi, J. He, T. M. Tritt, Materials Science and Engineering: R: Reports **97**, 1 (2015).

[59] Y. Pei, H. Wang, G. Snyder, Advanced Materials **24**, 6125 (2012).

[60] W. Kim, Journal of Materials Chemistry C **3**, 10336 (2015).

[61] G. Zhang, Y.-W. Zhang, in *Nanoscale Thermoelectrics*, edited by X. Wang, and Z. M. Wang (Springer International Publishing, Cham, 2014), p. 185.

[62] Wan, C., Wang, Y., Wang, N., Norimatsu, W., Kusunoki, M., & Koumoto, K. (2010). Development of novel thermoelectric materials by reduction of lattice thermal conductivity. Science and Technology of Advanced Materials, 11(4), 044306.

[63] A. Cantarero, F. X. Alvarez, in *Nanoscale Thermoelectrics* (Springer, 2014), p. 1.

[64] M. G. Kanatzidis, Chemistry of Materials **22**, 648 (2009).

[65] N. Satyala, P. Norouzzadeh, D. Vashaee, in *Nanoscale Thermoelectrics* (Springer, 2014), p. 141.

[66] M. Zebarjadi, K. Esfarjani, M. Dresselhaus, Z. Ren, G. Chen, Energy & Environmental Science **5**, 5147 (2012).

[67] A. Minnich, M. Dresselhaus, Z. Ren, G. Chen, Energy & Environmental Science **2**, 466 (2009).

[68] M. Steele, F. Rosi, Journal of Applied Physics **29**, 1517 (1958).

[69] V. A. Johnson, K. Lark-Horovitz, Physical Review **92**, 226 (1953).

[70] A. Middleton, W. Scanlon, Physical Review **92**, 219 (1953).

[71] D. M. Rowe, *CRC Handbook of Thermoelectrics* (CRC Press, 1995).

[72] J. Dismukes, L. Ekstrom, E. Steigmeier, I. Kudman, D. Beers, Journal of Applied Physics **35**, 2899 (1964).

[73] G. R. Schmidt, R. D. Abelson, R. L. Wiley, in SPACE TECHNOLOGY AND APPLICATIONS INT. FORUM-STAIF 2005: Conf. Thermophys in Micrograv; Conf Comm/Civil Next Gen. Space Transp; 22nd Symp Space Nucl. Powr Propuls.; Conf. Human/Robotic Techn. Nat'l Vision Space Expl.; 3rd Symp Space Colon.; 2nd Symp. New Frontiers (AIP Publishing, 2005), p. 295.

[74] C. Vining, *CRC Handbook of Thermoelectrics*, ed. Rowe, DM, CRC Press, Boca Raton, 328 (1995).

[75] H. Goldsmid, A. Penn, Physics Letters A **27**, 523 (1968).

[76] J. Parrott, Journal of Physics C: Solid State Physics **2**, 147 (1969).

[77] Z. Tan, W. Jesser, F. Rosi, Materials Science and Engineering: B **33**, 195 (1995).

[78] Cook, J. Harringa, S. Loughin, Materials Science and Engineering: B **41**, 280 (1996).

[79] Bhandari, D. Rowe, Journal of Physics C: Solid State Physics **11**, 1787 (1978).

[80] G. S. Nolas, J. Sharp, J. Goldsmid, *Thermoelectrics: basic principles and new materials developments* (Springer Science & Business Media, 2013), Vol. 45.

[81] R. Bunce, D. Rowe, Journal of Physics D: Applied Physics **10**, 941 (1977).

[82] C. B. Vining, W. Laskow, J. O. Hanson, R. R. Van der Beck, P. D. Gorsuch, Journal of Applied Physics **69**, 4333 (1991).

[83] T. Noguchi, *in Thermoelectrics*, 1997. Proceedings ICT'97. XVI International Conference on (IEEE, 1997), p. 207.

[84] D. Thompson, D. Hitchcock, A. Lahwal, T. Tritt, Emerging Mater Res **1**, 299 (2012).

[85] N. Mingo, D. Hauser, N. Kobayashi, M. Plissonnier, A. Shakouri, Nano Letters **9**, 711 (2009).

[86] M. Zebarjadi et al., Nano Letters **11**, 2225 (2011).

[87] G. Joshi et al., Nano Letters **8**, 4670 (2008).

[88] X. Wang et al., Applied Physics Letters **93**, 193121 (2008).

[89] A. Minnich, H. Lee, X. Wang, G. Joshi, M. Dresselhaus, Z. Ren, G. Chen, D. Vashaee, Physical Review B **80**, 155327 (2009).

[90] M. Haras, V. Lacatena, T. M. Bah, S. Didenko, J.-F. Robillard, S. Monfray, T. Skotnicki, E. Dubois, IEEE Electron Device Letters **37**, 1358 (2016).

[91] S. LeBlanc, S. K. Yee, M. L. Scullin, C. Dames, K. E. Goodson, Renewable and Sustainable Energy Reviews **32**, 313 (2014).

[92] J. P. Taborda, J. Romero, B. Abad, M. Muñoz-Rojo, A. Mello, F. Briones, M. M. Gonzalez, Nanotechnology **27**, 175401 (2016).

[93] A. A. Wilson, M. M. Rojo, B. Abad, J. A. Perez, J. Maiz, J. Schomacker, M. Martín-Gonzalez, D.-A. Borca-Tasciuc, T. Borca-Tasciuc, Nanoscale **7**, 15404 (2015).

[94] M. Hu, X. Zhang, D. Poulikakos, Physical Review B **87**, 195417 (2013).

[95] Y. D. Kuang, L. Lindsay, S. Q. Shi, G. Zheng, Nanoscale **8**, 3760 (2016).

[96] X. Gu, R. Yang, Journal of Applied Physics **117**, 025102 (2015).

[97] X. Zhang, H. Xie, M. Hu, H. Bao, S. Yue, G. Qin, G. Su, Physical Review B **89**, 054310 (2014).

[98] J. Reparaz, I. Marcus, A. Goñi, M. Garriga, M. Alonso, Journal of Applied Physics **112**, 023512 (2012).

[99] P. Ferrando-Villalba et al., Nano Research **8**, 2833 (2015).

[100] J. A. Perez-Taborda, M. Muñoz Rojo, J. Maiz, N. Neophytou, M. Martin-Gonzalez, Scientific Reports **6**, 32778 (2016).

[101] J.-K. Yu, S. Mitrovic, D. Tham, J. Varghese, J. R. Heath, Nature Nanotechnology **5**, 718 (2010).

[102] J. Tang, H.-T. Wang, D. H. Lee, M. Fardy, Z. Huo, T. P. Russell, P. Yang, Nano Letters **10**, 4279 (2010).

[103] E. Dechaumphai, D. Lu, J. J. Kan, J. Moon, E. E. Fullerton, Z. Liu, R. Chen, Nano Letters **14**, 2448 (2014).

[104] M. C. Wingert, S. Kwon, M. Hu, D. Poulikakos, J. Xiang, R. Chen, Nano Letters **15**, 2605 (2015).

[105] J. Chen, G. Zhang, B. Li, Applied Physics Letters **95**, 073117 (2009).

[106] J. J. Urban, Nature Nanotechnology **10**, 997 (2015).

[107] P. E. Hopkins, J. C. Duda, C. W. Petz, J. A. Floro, Physical Review B **84**, 035438 (2011).

[108] G. Chen, M. Dresselhaus, G. Dresselhaus, J.-P. Fleurial, T. Caillat, International Materials Reviews (2013).

[109] J. Wei, H. Liu, X. Tan, L. Cheng, J. Zhang, D. Fan, J. Shi, X. Tang, RSC Advances **4**, 53037 (2014).

[110] E. V. Jelenkovic, K. Tong, W. Cheung, S. Wong, B. Shi, G. Pang, Solid State Electron. **50**, 199 (2006).

[111] I. Nakamura, T. Ajiki, H. Abe, D. Hoshi, M. Isomura, Vacuum **80**, 712 (2006).

[112] W. Qin, D. G. Ast, T. I. Kamins, Journal of Applied Physics. **92**, 168 (2002).

[113] M. Lindorf, H. Rohrmann, G. Span, S. Raoux, J. Jordan-Sweet, M. Albrecht, Journal of Applied Physics **120**, 205304 (2016).

[114] M. Lindorf, H. Rohrmann, G. L. Katona, D. L. Beke, H. F. Pernau, M. Albrecht, Materials Today: Proceedings **2**, 557 (2015).

[115] M. Seibt, S. Buschbaum, U. Gnauert, W. Schröter, D. Oelgeschläger, Physical Review Letters **80**, 774 (1998).

[116] T. J. Konno, R. Sinclair, Philosophical Magazine B **71**, 163 (1995).

[117] Z. Wang, J. Wang, L. Jeurgens, E. Mittemeijer, Physical Review B **77**, 045424 (2008).

[118] K. U. M. Kumar, R. Brahma, M. G. Krishna, A. K. Bhatnagar, G. Dalba, Journal of Physics: Condensed Matter **19**, 496208 (2007).

[119] K. Kumar, M. G. Krishna, Journal of Nanomaterials **2008**, 57 (2008).

[120] S. Raoux, H.-Y. Cheng, J. L. Jordan-Sweet, B. Muñoz, M. Hitzbleck, Applied Physics Letters **94**, 183114 (2009).

[121] G. Gerlach, W. Dotzel, *Introduction to Microsystem Technology: A Guide for Students* (Wiley Microsystem and Nanotechnology) (Wiley Publishing, 2008).